

WIDESPREAD DISRUPTION OF RESONANT CHAINS DURING PROTOPLANETARY DISK DISPERSAL

BRAD M. S. HANSEN

Mani L. Bhaumik Institute for Theoretical Physics, Department of Physics & Astronomy, University of California Los Angeles,
Los Angeles, CA 90095

TZE-YEUNG YU

Mani L. Bhaumik Institute for Theoretical Physics, Department of Physics & Astronomy, University of California Los Angeles,
Los Angeles, CA 9009

YASUHIRO HASEGAWA

Jet Propulsion Laboratory, California Institute of Technology, Pasadena, CA, 91109

Version July 22, 2024

ABSTRACT

We describe the evolution of low mass planets in a dispersing protoplanetary disk around a Solar mass star. The disk model is based on the results of Yu et al. (2023), which describes a region of the inner disk where the direction of the migration torque is outwards due to the diffusion of the stellar magnetic field into the disk and the resultant gradual increase in surface density outwards. We demonstrate that the magnetospheric rebound phase in such a disk leads to diverging orbits for double and triple planet systems, and the disruption of a high fraction of the initial resonant chains.

We present simulations of three planet systems, with masses based on the observed triple planet systems observed by the Kepler satellite, within the context of this model. The final distribution of nearest neighbour period ratios provides an excellent fit to the observations, provided that the initial configurations contain a significant fraction of pairs whose period ratios are less than 2:1. The occurrence rate of planets as a function of orbital period also provides a good match to the observations, for final orbital periods $P < 20$ days.

These results suggest that the period and period ratio distributions of low mass planets are primarily set in place during the disk dispersal epoch, and may not require significant dynamical evolution thereafter.

1. INTRODUCTION

The Kepler satellite mission (Borucki et al. 2010) has revealed that $> 50\%$ of Sun-like stars possess planetary systems containing at least one and, frequently, several planets with orbital periods < 100 days (Batalha et al. 2013; Coughlin et al. 2016; Lissauer et al. 2023). The majority of these planets have masses that lie between those of Earth and Saturn, suggesting a commonality with either rocky planets (hereafter Super-Earths) or planets with a substantial gaseous or water content by mass (hereafter Sub-Neptunes). Despite their widespread occurrence, the origins of these planets is still a matter of lively debate.

One school of thought suggests that such planets, especially those with volatile-rich envelopes, formed further from the star and migrated inwards due to interactions with the gaseous protoplanetary disk. The migration timescales associated with low mass planets are quite short, but gravitational interactions between multiple migrating planets can slow the evolution sufficiently to avoid losing the planets into the central star (Terquem & Papaloizou 2007; Ida & Lin 2008, 2010; Hellary & Nelson

2012; Cossou et al. 2014; Coleman & Nelson 2014; Izidoro et al. 2017). The high frequency of multiple planet systems also aligns nicely with this model. However, such models predict a high occurrence rate of mean motion resonances in such systems, which is not matched by observations (Lissauer et al. 2011; Fabrycky et al. 2014). An alternative class of models suggests that the planets assembled in situ, with little radial migration (Hansen & Murray 2012; Chiang & Laughlin 2013; Boley et al. 2014; Chatterjee & Tan 2015). These models can better match the observed spacing of planets in multiple systems (Hansen & Murray 2013), but require that the protoplanetary disks be either unusually massive or allow for significant inward migration of solid material as small bodies, prior to assembly.

For models in which the planets migrate within the protoplanetary disk, a critical element is the process that determines the halting of migration. In particular, the structure of the inner edge of the disk is expected to be regulated by the interaction with the stellar magnetic field (Romanova & Lovelace 2006; Romanova et al. 2019) and the change in the density structure reduces or reverses the torque driving the planets inwards (Masset et al. 2006; Tsang 2011; Miranda & Lai 2018). For the

purposes of modelling migration, this is often presented as a simple truncation in surface density, resulting from the balance of the ram pressure of the disk flow with the magnetic pressure of the magnetic field (Terquem & Papaloizou 2007; Chang et al. 2010; Izidoro et al. 2017; Brasser et al. 2018). However, Yu et al. (2023) have shown that a more accurate model, that accounts for the diffusion of the magnetic field into the disk, will result in a surface density that increases outwards from the inner edge before reaching a maximum and reverting to a more traditional power-law decay to larger radii. The change in the surface density and temperature profiles reverses the torque direction interior to the surface density maximum. Thus, migrating planets reverse the course of their migration as they cross this transition and pile up, not at the edge of the magnetospheric cavity, but at a more distant location – the surface density maximum. As the accretion rate drops, the torque reversal location moves outwards, causing the planet to move outwards again, coming to rest at the point where the disk density has dropped to the point that the migration ‘freezes out’.

In Yu et al. (2023) we demonstrated how this model determines the final orbital periods in the case of a single planet. In this paper, we wish to investigate the consequences of this model for multiple planet systems. An important feature of the multiple planet case is that it can result in planetary pairs breaking out of resonance. Liu et al. (2017) have shown that, as the accretion rate drops, the magnetospheric cavity expands and can drive outward migration of a planet trapped at the inner edge. They use a one-sided torque operating at the disk edge, based on the results of the studies above. The fact that outward torques operate only on one planet in that model limits the degree to which this effect operates to disrupt a resonance chain, and the resulting simulations still leave too many systems in resonant configurations (Liu & Ormel 2017). As we will show, the presence of a non-zero torque interior to the location of the torque reversal results in multiple planets migrating outwards and provides a more extensive dynamical perturbation to the system.

In this paper we present a calculation of the resonant dynamics of two and three planet systems, evolving under the influence of a torque model adapted from Yu et al. (2023). The dynamical model, including both resonant interactions and torques from the protoplanetary disk, is described in §2. In §3 we adapt the semi-analytic treatment of the resonant dynamics to take into account the torque reversals. §4 presents the application of our model to two planet systems and describes the character of the evolution over the range of planetary masses. In §5 we show how the introduction of a third planet influences the dynamics and present a comparison between model results and the Kepler observational sample. The implications of our results are discussed in §6.

2. DYNAMICAL MODEL

We wish to model the resonant dynamics of two and three planet systems, under the influence of the most important resonant interactions. We choose to focus on the first order resonances $(q + 1)/q$ where $q = 1$ and $q = 2$. We will also include the effects of torques from the protoplanetary disk on both semi-major axis evolution and planetary eccentricity damping. This is done by includ-

ing, in the equations, a linear decay term characterised by a timescale, as has been done by several prior authors – (Terquem & Papaloizou 2019; Choksi & Chiang 2020). One difference in our case is that our torque is based on the model of Yu et al. (2023), which features a reversal of the torque direction in the inner disk, due to the penetration of the stellar magnetic field into the disk. We must therefore allow for the timescale for semi-major axis evolution (τ_a) to become negative, in order to allow for outward migration. The timescale for eccentricity damping is always positive. The equations featuring three planets and two resonances are sufficiently lengthy that we defer their explicit expression to Appendix A.

2.1. Torque Model

The dynamical evolution of the system is driven by the torques exerted by the protoplanetary disk. We determine a functional form for the torque based on a fit to the numerical disk simulations discussed in Yu et al. (2023). For the inward migration, the characteristic timescale for semi-major axis evolution of planet i is

$$\tau_{a,i} = 0.36 \text{Myr} \left(\frac{a_i}{0.1 \text{AU}} \right)^{1.38} \left(\frac{M_i}{10 M_{\oplus}} \right)^{-1} \left(\frac{\dot{M}}{1.8 \times 10^{-9} M_{\odot}/\text{yr}} \right)^{-0.85} \quad (1)$$

where a_i is the semi-major axis, M_i is the planetary mass, and \dot{M} is the rate of mass accretion through the disk (assuming a central star of $1 M_{\odot}$). The time dependence of τ_i is driven by the evolution of the accretion rate, which is

$$\dot{M} = \frac{2.5 \times 10^{-8} M_{\odot} \text{yr}^{-1} \exp(-t/0.63 \text{Myr})}{1 + \exp((t - 1.7 \text{Myr})/0.15 \text{Myr})}. \quad (2)$$

This is chosen to represent a disk that decays exponentially with time t as it accretes onto the star but then cuts off more rapidly once photoevaporation losses detach the inner disk from mass resupply by the outer disk (Alexander et al. 2014).

Once a planet has crossed interior to the torque reversal line a_R – located at the disk surface density maximum (Yu et al. 2023), the migration torque is now directed outwards. We describe this using a negative timescale. The functional form is again determined by fitting to the simulations of Yu et al. (2023), and is expressed as a function of position relative to a_R , $z = \ln a_i - a_R$. This amounts to

$$|\tau_{a,i}| = 6.66 \times 10^{-18} \text{Myr} \left(\frac{0.1 \text{AU}}{a_i} \right)^{1/2} \left(\frac{10 M_{\oplus}}{M_i} \right) \left(\frac{\dot{M}}{1.8 \times 10^{-9} M_{\odot}/\text{yr}} \right)^{-1.8} e^{-(120.04 + 177.76z + 65.5z^2 + 8.07z^3)} \quad (3)$$

These quantities are furthermore linked by the fact that the transition radius a_R is, itself, a function of \dot{M} and thus of time, with

$$a_R = 0.062 \text{AU} \left[1 + 0.229 \ln \left(\frac{\dot{M}}{2.5 \times 10^{-8} M_{\odot}/\text{yr}} \right) \right]^{-1} \quad (4)$$

in the case of our default model¹. Indeed, if the migration time inward or outward is shorter than the timescale on which a_R is evolving, then the planet will track the torque reversal location, making the relevant characteristic timescale $\tau_R = dt/d \ln a_R$.

For example, if the outer planet of the pair reaches the torque reversal location, then the pair of planets will both be migrating outwards. The question of whether they converge or diverge will rest on whether the outward migration of the inner planet is faster or slower than the rate at which a_R recedes because the outer planet is locked to a_R by the fact that the torques on either side of this transition drive the planet towards it. Two examples of this evolution are shown in Figure 1. The solid curve shows the characteristic timescale $|\tau_R|$ associated with the outward movement of the torque reversal location as \dot{M} decreases. We also show two cases of $|\tau_{a,i}|$ interior to this. The dotted line shows the rate of outward migration for a $6M_\oplus$ planet that is the interior member of a pair locked in the 2:1 mean motion resonance, in which the outer member is located at a_R . At early times, $|\tau_{a,i}| < |\tau_R|$, so that the planet is able to keep up with the outward migration of the outer member of the pair (which is tied to the torque reversal location a_R). Thus, the pair is converging and remains trapped in resonance, even during the outward migration. Figure 1 shows that $|\tau_{a,i}|$ increases with time, while the solid curve ($|\tau_R|$) decreases with time. Therefore, when these two curves cross, the inner planet falls behind and the pair starts to diverge, falling out of resonance.

The dashed line shows the case of a $3M_\oplus$ planet locked in a 3:2 resonance with an outer member located at a_R . This shows the same characteristic behaviour, although the divergence starts earlier. The long dashed curve shows the inward migration timescale for a planet located just exterior to a_R . The fact that this curve falls below the others means that the outer member of the pair remains locked to a_R even as the inner member drops out of resonance, although eventually this planet falls behind the retreat of a_R as well.

The specific value of a_R also depends on the stellar magnetic field and the degree to which it diffuses into the disk. For a simple dipole field ($n=3$), equation (4) is equivalent to a magnetic field on the stellar surface of 300 G. The magnetic fields observed in T Tauri stars can reach several kG (Johns-Krull 2007) but many stars also show smaller or unobservable fields (Donati et al. 2011; Villebrun et al. 2019). Furthermore, Yu et al. (2023) showed that the results of the disk simulations scaled with the enclosed magnetic flux within the planetary radius. Thus, equation (4) also represents a surface field of $B_0 = 1.7$ kG with an effective $n=3.5$. Given this ambiguity in trading off B_0 and n , and the range of potential natal stellar fields, we shall investigate the effects of varying magnetic field by simply scaling the value of a_R in subsequent sections.

A full description of the interaction between the star and the disk must also account for the fact that there is a true inner boundary at the edge of the magnetospheric cavity. In most of the cases we discuss here, the planets do not penetrate in far enough to reach this boundary,

¹ We set the maximum value of $a_R = 1$ AU. The exact value is not important as the migration freezes out long before this occurs.

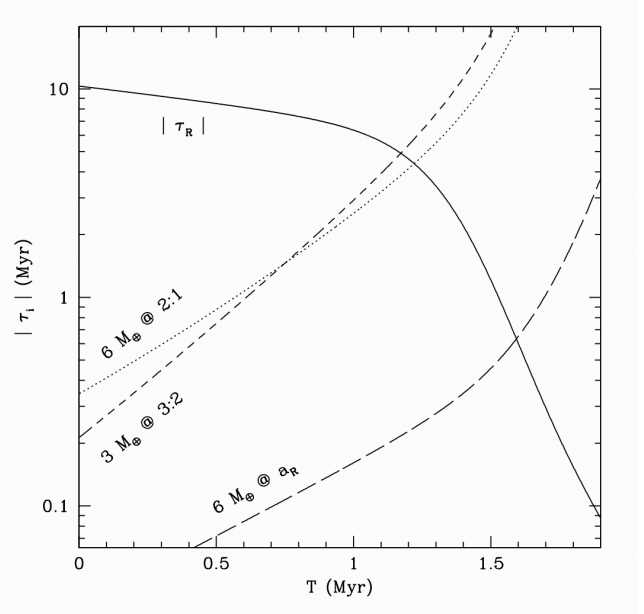


FIG. 1.— The solid curve shows the characteristic timescale for the evolution of a_R as a function of time. We see that this is initially much longer than the lifetime of the disk, but shortens as time increases, i.e. the torque reversal moves out faster as \dot{M} drops. The dotted curve represents $|\tau_i|$ at a location $0.63a_R$, assuming a mass $6M_\oplus$. This represents the rate of outward migration for a planet of that mass, trapped in a 2:1 resonance with a planet located at the torque reversal location. The dashed line represents the same but for a $3M_\oplus$ planet located at $0.763a_R$, i.e. in a 3:2 resonance. Both timescales are shorter than $|\tau_R|$ until about 1.2 Myr. After this, the planets cannot keep up with a_R and will freeze out and decouple from the disk. The long dashed line indicates the timescale for inward migration, evaluated at a_R . This is shorter than the timescales for the inner planet, indicating that the outer member of the pair will freeze out at a later time.

and so we will simply consider the magnetospheric cavity to lie at $a_R/3.7$ unless otherwise noted.

In the following sections, we calculate the evolution of two and three planet systems evolving according to these torques. In addition to the decay of the semi-major axis, these torques also damp eccentricities. Resonant interactions between neighbouring planets lead to a coupled evolution, including eccentricity excitation and resonant lock. The equations that describe this evolution are given in Appendix A.

3. CONVERGING VERSUS DIVERGING

When two planets converge during migration, they enter a state of resonant lock, in which the rate of change of orbital frequencies are equal, i.e. $\dot{n}_1/n_1 = \dot{n}_2/n_2$. If we simultaneously impose the condition that the libration amplitude of the resonant angle is small, the eccentricities reach equilibrium values given by (Terquem & Papaloizou 2019), in the ratio

$$\left(\frac{e_2}{e_1}\right)^2 = \frac{1}{4} \left(\frac{m_1}{\alpha_{12}m_2}\right)^2 \left(\frac{f_2''}{f_1}\right)^2 \quad (5)$$

where we have chosen the $q=1$ resonance for this example and the various quantities are defined using the conventions given in appendix A. These conditions also imply specific values for the equilibrium eccentricities. The full expressions are given in Terquem & Papaloizou (2019),

but the most important element is that

$$e_1^2 \propto \left(\frac{t_{e,1}}{t_{a,2}} - \frac{t_{e,1}}{t_{a,1}} \right) \quad (6)$$

In the traditional case where both planets are migrating inwards, this quantity is positive as long as $t_{a,1} > t_{a,2}$, i.e. convergent migration yields resonant lock. In our model, the torques can reverse sign, which can be modelled as simply reversing the sign of the relevant timescale.

Thus, when the innermost planet first crosses the torque reversal location, the value of $t_{a,1}$ will change sign. This will cause the pair to converge even more strongly, so that there will still be an equilibrium, although the values of the equilibrium eccentricities will change. This can occur even if the resonant lock does not change. However, once the second planet crosses the torque reversal location, then both planets are moving outwards and the question of whether they are converging or diverging is once again a matter of their relative motion. The equilibrium will fail if the quantity in equation (5) becomes negative – thereby breaking the resonant lock. The system evolution retains the same character if one of the planets is tracking the location of the torque reversal – the relative t_a is then simply dictated by τ_R – the evolution of the torque reversal.

Extending the analysis to three planet systems yields qualitatively similar behavior, with locked resonant systems exhibiting equilibrium eccentricities in fixed proportions, but also demonstrating failure of these equilibria once the planets start to move outwards again.

4. TWO PLANET SYSTEMS

Figure 2 illustrates the basic evolution for a two planet system, containing two $3M_{\oplus}$ planets. The initial semi-major axes are 0.076 AU and 0.1 AU, with initial eccentricities of 0.01. The initial mean longitudes and longitudes of periastron were chosen randomly and the relevant resonant angles constructed therefrom. The equations in Appendix A are integrated using the adaptive stepsize integrator *odeint* from Press et al. (1992). The black curve in the upper left plot illustrates the evolution of the semi-major axis of the inner planet, and the red curve the evolution of the outer planet. The dotted line indicates the evolution of the location of the torque reversal a_R . The upper right panel shows the period ratio of the two planets as a function of time. In the lower left, we show the evolution of the planetary eccentricities, and, in the lower right, the panel shows how the resonant angle for the inner and outer 3:2 resonances change with the planetary and disk evolution.

The first incident of note – denoted point A – is when the inner planet reaches the torque reversal location a_R . At this point the inward migration of the inner planet stops and the planet semi-major axis starts to track the evolution of a_R , which is slowly moving outwards. Up until this point, the period ratio is increasing (the planets are diverging) because the migration time decreases as planets get closer to the star. However, with the halting of the inner planet migration at A, the planets begin to converge because the outer planet, shown as the red curve, continues to migrate inwards, and the two planets enter the 3:2 resonance at B. The net relative motion is convergent and so the pair become locked in a resonant

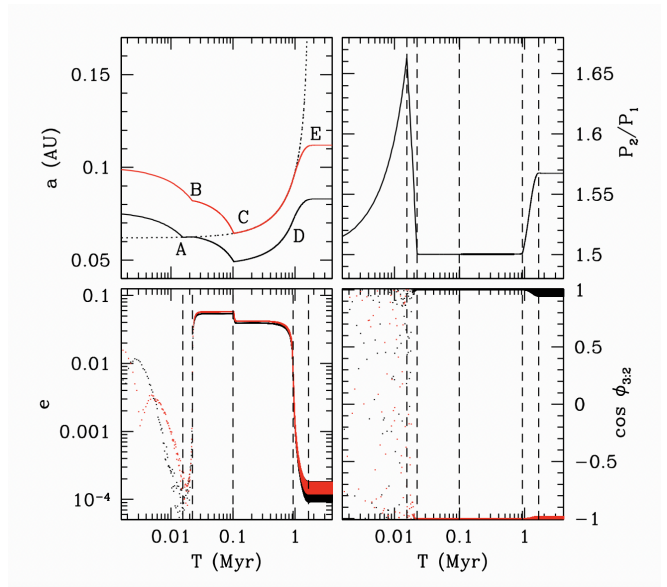


FIG. 2.— The upper left panel shows the evolution of semi-major axis for a pair of $3M_{\oplus}$ planets migrating due to the gaseous torque model described in the text. The dotted curve shows how the location of the torque reversal evolves with time. Important transitions in the dynamical state of the system are labelled A–E, and are shown as vertical dashed lines in the other three panels. In the upper right, we see the evolution of the period ratio for the pair. In the lower left we show the evolution of the eccentricity for each planet (red curve indicating the outer planet and black curve the inner planet). In the bottom right, we see the evolution of the cosines of the resonant angles $\phi_{3:2}$, namely $3\lambda_2 - 2\lambda_1 - \bar{\omega}_1$ (black) and $3\lambda_2 - 2\lambda_1 - \bar{\omega}_2$ (red).

configuration. As a result, the eccentricities rise from almost zero to finite values dictated by the equilibrium defined by equation (5).

The torques on the outer planet now drive the pair inwards, and the inner planet is pushed interior to the torque reversal. Eventually the outer planet reaches the torque reversal (at time denoted as C). The planets remain in equilibrium (because the torques on the inner planet are pushing it outwards, so the pair is still converging) but the equilibrium eccentricities change because the sign of the torques change which changes the equilibrium condition in equation (6). After this, the pair starts to migrate outwards but remains in resonance as long as the rate of outward migration of the inner planet is faster than the evolution of the torque reversal. This continues for a long time, but eventually, as the torques weaken and the outward motion of a_R accelerates, the pair starts to diverge, at epoch D. The libration in the 3:2 resonance begins to increase, as does the period ratio, and the eccentricities start to damp away as their resonant excitation weakens. Eventually the migration freezes out completely (at E), leaving the system still in resonance with a finite libration amplitude and an offset relative to strict commensurability.

This is the fundamental result that emerges from these calculations – in the disk models of Yu et al. (2023), planets are not trapped at the true inner edge of the disk, but rather at the location of the torque reversal. As the disk evolves and the surface density drops, this location moves outwards, resulting in an outward migration of the planets at, and interior to, the torque reversal. In many cases, this leads to divergent migration, thereby

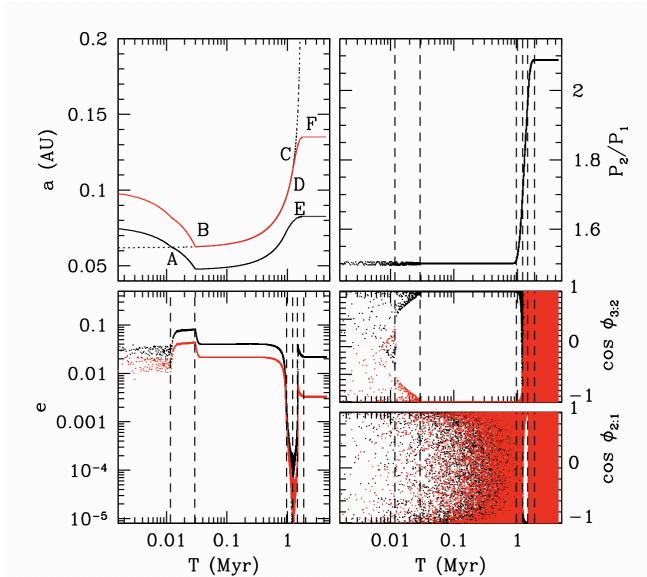


FIG. 3.— The upper left panel shows the evolution of semi-major axis for a pair of migrating planets where the outer planet is $6M_{\oplus}$ and the inner planet is $3M_{\oplus}$. The dotted curve shows how a_R evolves with time. Important transitions in the dynamical state of the system are labelled as A–F, and are shown as vertical dashed lines in the other three panels. In the upper right, we see the evolution of the period ratio for the pair. In the lower left we show the evolution of the eccentricity for each planet (red curve indicating the outer planet and black curve the inner planet). In the bottom right, we have two panels to track the evolution of the cosines of the resonant angles for the two important first order resonances that are encountered. The one designated as $\phi_{3,2}$ shows the angles $3\lambda_2 - 2\lambda_1 - \bar{\omega}_1$ (black) and $3\lambda_2 - 2\lambda_1 - \bar{\omega}_2$ (red). The one designated as $\phi_{2,1}$ shows the evolution of the two resonant angles $2\lambda_2 - \lambda_1 - \bar{\omega}_1$ (black) and $2\lambda_2 - \lambda_1 - \bar{\omega}_2$ (red).

breaking the resonant lock and causing divergence of the period ratios away from the initial commensurabilities.

The planetary masses also play a role in determining the outcome of the evolution, because more massive planets remain coupled to the gas disk for longer, and lower mass planets freeze out earlier. To illustrate this, Figure 3 shows the case of a two planet system wherein the outer planet ($6M_{\oplus}$) is more massive than the inner one ($3M_{\oplus}$). The initial semi-major axes, eccentricities and longitudes are the same as in Figure 2 and the initial evolution is qualitatively similar, except that the stronger torques on the outer planet means that the inner planet barely halts at the torque reversal before being captured in resonance and pushed further inwards. The eventual divergence from the 3:2 resonance (at D) is also qualitatively similar. However, the outer planet remains coupled to the gas disk for longer by virtue of its larger mass and so migrates far enough that the system passes through the 2:1 resonance (shown at D). This resonant encounter is now divergent, so there is no capture (the system leaves the 2:1 resonance at E) but there is a transient excitation of the eccentricities that occurs late enough to leave small non-zero eccentricities (~ 0.01) after the system has frozen out (at F).

The overall amount of migration is driven largely by the planetary masses, as they determine how long the planet remains coupled to the disk and how rapidly the planets migrate with respect to one another. Figure 4 shows the effect of both planetary mass ratio and to-

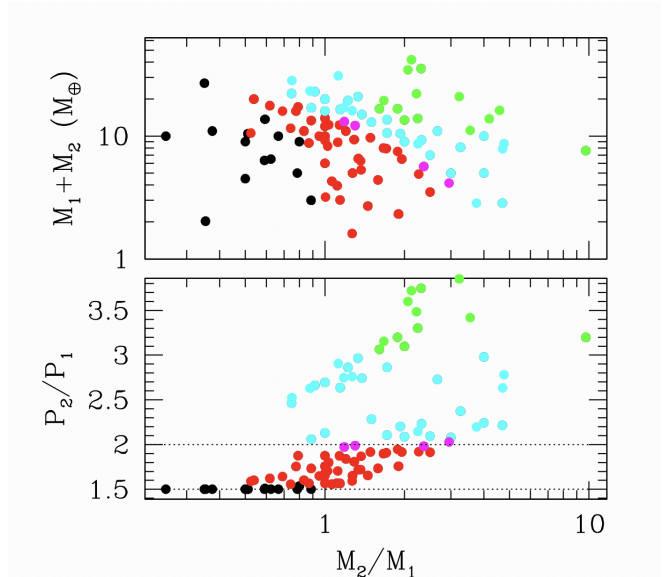


FIG. 4.— The lower panel shows the final period ratio of a planetary pair as a function of the mass ratio M_2/M_1 . The results are color coded according to the final value, with black signifying $P_2/P_1 < 1.55$, red (1.55–1.95), magenta (1.95–2.05), cyan (2.05–3) and green for $P_2/P_1 > 3$. In the upper panel, these colors indicate the final states of systems as a function of mass ratio and total system mass $M_1 + M_2$. The dotted lines in the lower panel indicate the first order commensurabilities $(1+q)/q$ for $q=2$ and $q=1$.

tal mass in the overall evolution of a range of planet pairs. Each pair starts with the same semi-major axes and eccentricities as in Figure 2, while the initial mean longitudes and longitudes of periastron are chosen randomly. We see that low mass ratios ($M_2/M_1 < 0.6$) leave pairs trapped in the original 3:2 resonance, whereas larger mass ratios lead to divergence and a wide range of final period ratios, including some in the range of the wider 2:1 resonance. This is a consequence of the fact that the more massive planets remain coupled to the gas for longer. Thus, if the inner planet is the more massive one, the pair will remain in the convergent state for the entirety of the disk evolution. However, if the outer planet is the more massive one, then the inner planet will freeze out first and fall behind the outer planet’s migration. This leads to a diverging configuration and a final period ratio that increases as M_2/M_1 does. The degree of divergence also depends on the total planet mass, with more massive planetary systems leading to large final mass ratios (because they remain coupled to the disk for longer).

4.1. Dependence on model parameters

The evolution of these planetary pairs is driven by the torques due to the gas disk, so they will be influenced by the parameters of the gaseous disk, and also by the strength of the stellar magnetic field – which determines the location of the torque reversal that drives the outward motion and divergence. Figure 5 illustrates this.

Figure 5 shows the evolution of a pair of $6M_{\oplus}$ planets in three different scenarios. In each case, the accretion disk evolution is the same, but we have scaled the form of a_R , given in equation (4), by a constant factor. As discussed above, this mimics variations in either the stellar magnetic field strength, or the degree of field compres-

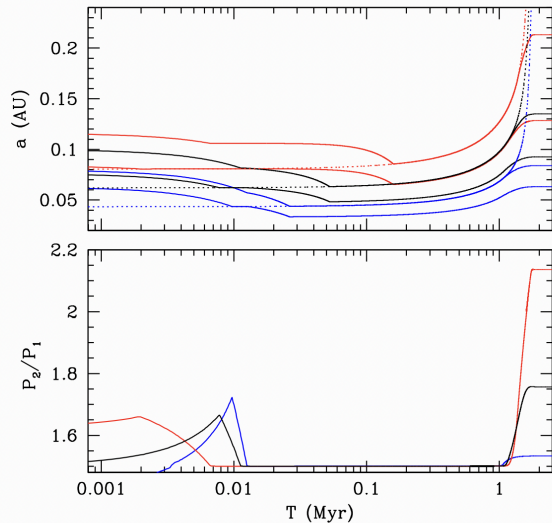


FIG. 5.— The upper curves show the evolution of the semi-major axes of pairs of $6M_{\oplus}$ planets evolving in disks with different torque reversal locations (a_R). The black curve corresponds to the model given by equation (4). The red curves correspond to a_R scaled up by a factor 1.3, and the blue curves have a_R scaled down by 0.7. The dotted lines show the evolution of the respective a_R . The lower panel shows the evolution of the corresponding period ratios.

sion by the inflow (n). Thus the black curve in Figure 5 shows the default case, while the blue curve shows the case where a_T is a factor 0.7 smaller (corresponding to a weaker magnetospheric influence) and the red case represents the case where a_T is a factor 1.3 larger (corresponding to a stronger magnetospheric influence). In each case, the initial semi-major axes are chosen such that all planets start exterior to a_R . The blue curves start with semi-major axes 0.063 and 0.08 AU, the black curves with 0.076 and 0.1 AU, and the red curves with 0.084 AU and 0.116 AU. Initial eccentricities are still 0.01 and longitudes are chosen at random.

We see that more distant torque reversals result in an earlier entry into resonance, and a slightly later departure from commensurability. The end result is a more widely separated pair of planets. Given that we expect a range of stellar magnetic fields amongst exoplanet host stars, this will also result in some variation of the planetary spacings.

The final separations also depend on the model for the evolution of the accretion rate and surface density of the disk. Our default model assumes an evolution characterised by two exponentials, chosen to mimic the slow decay of a viscously evolving disk that accelerates once the inner disk has been decoupled from the outer disk by photoevaporation. Figure 6 shows how the evolution of a pair of $6M_{\oplus}$ planets changes depending on the choice of the faster exponential cutoff. Initial conditions for each case are the same as those for Figure 2. We show the evolution where the cutoff rolls over after 1.7 Myr, 1.9 Myr or not at all (i.e. the decay is characterised by only one exponential – the slower one). We see that later cutoffs lead to more divergence.

5. THREE PLANET SYSTEMS

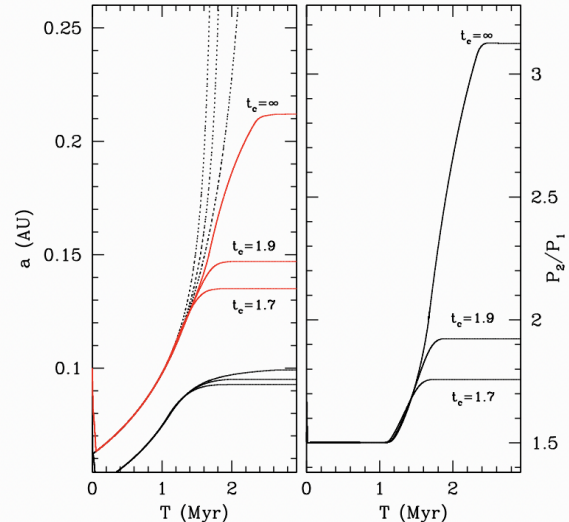


FIG. 6.— The curves show the evolution of a pair of $6M_{\oplus}$ planets in the same disk, with the same initial conditions, but with three different values for the time (t_c) at which the accretion rate starts to rapidly drop off. In the left panel, the three black curves represent the inner planet and the three red curves the outer planet. The right hand panel shows the evolution of the respective period ratios.

In the previous section, we have demonstrated that the presence of a transition region and torque reversal in the inner disk can cause a significant dynamical shake-up in planetary systems, potentially explaining the low frequency of observed resonant pairs. The sample of planets discovered by the Kepler satellite contains many systems with multiplicity higher than two. In this section we will examine the effects of a torque reversal on three planet systems.

The addition of a third planet adds some complexity to the system, as the planet in the middle now experiences gravitational interactions from both the inner and outer companions. As a result, this planet may be evolving outwards with the torque reversal – and diverging from the inner planet – but then experiences torques from the third, outer, planet, which is still being driven inwards. This influence can counter the evolution discussed in the previous section, and so we must consider the parameters associated with this competition.

Figure 7 shows the simple extension of our model system shown in Figure 2, in which we simply add a third planet, also of mass $3M_{\oplus}$. The initial semi-major axes are now 0.08, 0.107 and 0.149 AU, chosen so that both pairs begin between the 3:2 and 2:1 commensurabilities. Eccentricities and longitudes are chosen as before. The initial evolution is divergent, because the rate of migration is faster closer to the star. The first planet encounters the torque reversal at A, and so the inner pair begins to converge, trapping into the 3:2 resonance at B. This excites the eccentricities of the inner pair to equilibrium values, but the outer planet remains almost circular as it continues to migrate inwards. The resonant interaction slows the inward migration of the middle planet and the outer pair encounters the 3:2 resonance at C. This also briefly disturbs the resonance lock of the inner pair, but both pairs soon settle into resonance again when the

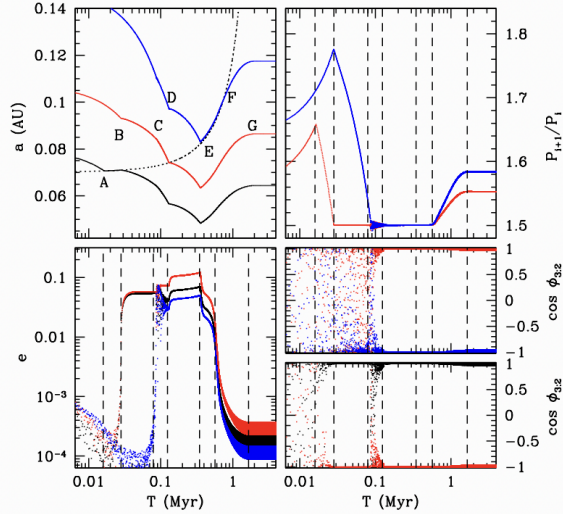


FIG. 7.— Here we show a three planet system, containing three planets, each with mass $3M_{\oplus}$. The evolution of the inner planet is shown in black, the middle planet in red, and the outer planet in blue. In the upper right panel, the red curve refers to period ratio of the inner pair, while the blue curve indicates the period ratio of the outer pair. In the lower right, we show the behaviour of the cosines of the resonant angles for the 3:2 resonance for both the outer pair (red and blue) and inner pair (red and black). The labels in the upper left indicate important epochs in the evolution of the system, identified as vertical dashed lines in the other panels.

middle planet reaches a_R (at D), along with a new set of equilibrium eccentricity ratios. The outer planet continues to migrate inwards, pushing both the inner and middle planets interior to a_R , until it eventually encounters the torque reversal as well (at E). At this point we have three planets in a resonant chain of 3:2 resonances, moving outwards with the outer planet tracking a_R . As we have noted above, this will continue until the evolution of a_R accelerates and the planets start to diverge (at F). The divergence is not rapid, and the planets eventually freeze out (at G) still in resonance, with a small libration, and moderate separations from commensurability.

The end result is a trio of planets, with the inner pair having period ratio $P_2/P_1 = 1.54$, and the outer pair with a period ratio $P_3/P_2 = 1.57$ – similar to what one would expect by simply combining the two pairs independently.

Figure 8 shows the effect of more massive planets and wider orbits. All the masses are scaled up by a factor of 2 – i.e. a system containing three planets of mass $6M_{\oplus}$. Initial semi-major axes are 0.076, 0.107 and 0.223 AU, so that the outer pair starts wide of the 2:1 resonance. The inner pair evolves in the same manner as before – converging after the inner planet reaches the torque reversal (A), locking into the 3:2 resonance (B) and finding a new equilibrium when the middle planet reaches the torque reversal (D). However, the larger masses mean that the outward torque is stronger and the mutual gravitational interactions are strong enough to prevent the outer planet from forcing its way inward to a_R . Thus, the system evolves for a period of time with the middle planet tracking a_R and maintaining an inner 3:2 and outer 2:1 resonance, with the outer planet being driven outwards despite not

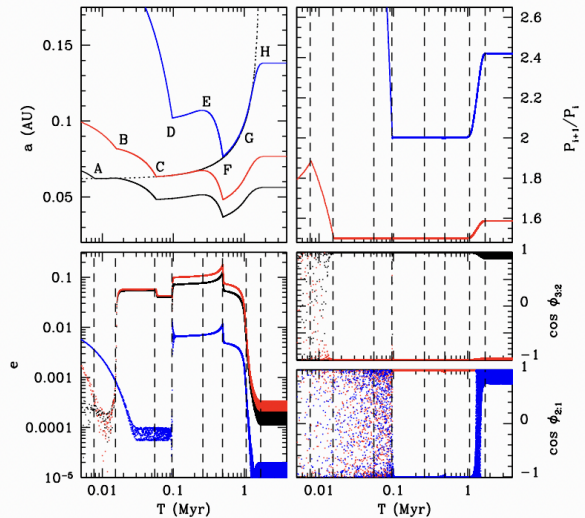


FIG. 8.— Here we show a three planet system, containing three planets, each with mass $6M_{\oplus}$. The evolution of the inner planet is shown in black, the middle planet in red, and the outer planet in blue. In the upper right panel, the red curve refers to period ratio of the inner pair, while the blue curve indicates the period ratio of the outer pair. In the lower right, we show the behaviour of the resonant angles for the different first order resonances at play. The upper panel in this quadrant shows the evolution of the cosine of the resonant angle for the 3:2 resonance for the inner pair (red and black). The bottom panel show the corresponding evolution for the 2:1 resonance between the outer pair of planets. The labels in the upper left indicate important epochs in the evolution of the system, identified as vertical dashed lines in the other panels.

having reached a_R .

Eventually, as the outwards evolution of a_R accelerates, the middle planet detaches from the torque reversal and the outer planet resumes its inward migration (E), eventually reaching a_R at F. At this point the evolution is similar again, with the planets starting to diverge from strict commensurability as the outer planet decouples from the torque reversal (G) and eventually freezing out at H. One noteworthy difference here though, is the behaviour of the outer pair, wherein the outer 2:1 resonant angle reverses its libration orientation. This occurs when the period ratio diverges beyond $P_3/P_2 = 2.25$, at which point the stable libration equilibrium switches in angle by π (as discussed in appendix A).

5.1. Observational Comparison

These calculations demonstrate that the evolution of systems of multiple planets in the protoplanetary disk background calculated by Yu et al. (2023) can produce divergence from resonance and result in final period ratios well away from the commensurabilities expected in a naive application of the resonant locking theory.

In a perfect scenario, we should be able to model the divergence of specific planetary systems with well-defined masses, although the stellar magnetic field value and the evolution of the protoplanetary disk remain quantities that need to be modelled and so can introduce some variations. Of course, the observational reality is less well constrained – most of the known multiplanet systems are detected via the transit method, and most of the plan-

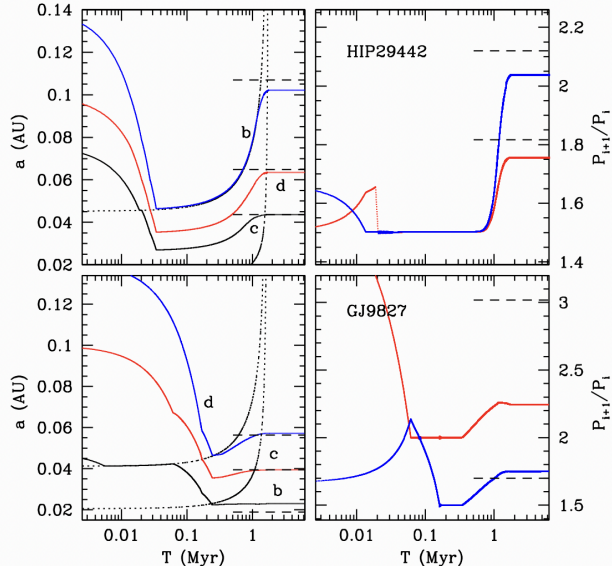


FIG. 9.— The curves in the upper two panels show the evolution of a planetary system modelled after the HIP29442 planetary system, assuming our standard disk and a torque reversal scaled by a factor 0.73. The horizontal dashed lines in the left hand panel indicate the observed final semi-major axes and the horizontal dashed lines in the upper right panel indicate the observed final period ratios. The lower panels show the equivalent evolutions for the GJ9827 system, in which the torque reversal is scaled by 0.55. In both panels, the upper dotted line indicates the torque reversal a_R , while the lower dotted line indicates the edge of the magnetospheric cavity, where the torques go to zero.

etary masses are small enough to prove challenging to measure with the radial velocity method.

Nevertheless, it is instructive to compare our existing model with the few known planetary systems where the planetary masses are well measured. As a comparison for our model, we require systems of three planets, orbiting approximately Solar-mass stars, and with well measured masses. We restrict ourselves solely to triple planet systems, since the presence of neighbors does influence the degree of divergence.

Figure 9 shows a comparison for the two planetary systems that best match our criteria. In the top panel we show a model for the planetary system around the star HIP29442. This system has a host star that is close to solar mass ($0.89M_{\odot}$), and has exactly three planets with well-constrained masses (errors $< 1M_{\oplus}$). In the bottom panel, we show a comparison to the star GJ9827. The host star in this system is $0.62M_{\odot}$, which is probably too low to be strictly applicable to our model, but is the next closest match and still instructive. Other systems with well measured masses either orbit M dwarfs or have either more or less than three planets.

The planetary masses for HIP29442 measured by Damasso et al. (2023) are $4.5 \pm 0.3M_{\oplus}$, $5.1 \pm 0.4M_{\oplus}$ and $9.6 \pm 0.8M_{\oplus}$ for the three planets with orbital periods of 3.538 days (c), 6.429 days (d) and 13.63 days (b). To model this system we choose the scaling of a_R so that the innermost planet freezes out at approximately the correct distance. The initial semi-major axes are 0.076, 0.1 and 0.14 AU, with initial eccentricities of 0.01 and random initial longitudes. The resulting evolution shows the system enters a 3:2+3:2 resonant chain early and

then diverges to final period ratios that are similar to those observed, although slightly smaller. In particular, we note that the outer pair diverged from interior of the 2:1 resonance to outside it.

The masses for the GJ9827 planets (Passegger et al. 2024) are $4.3 \pm 0.3M_{\oplus}$, $1.9 \pm 0.4M_{\oplus}$ and $3.0 \pm 0.6M_{\oplus}$, corresponding to orbital periods of 1.209 days (b), 3.648 days (c) and 6.202 days (d). In this case, we scaled a_R so that the middle planet freezes out at the correct distance, and scaled the accretion rate down by a factor of 0.7 to account for the lower stellar mass. The initial conditions are the same as for HIP29442 except that the inner planet starts with semi-major axis 0.048 AU so that it encounters a_R early – since the observed inner planet is very close to the host star. With these adjustments our migration model is able to match the outer pair quite well, but the inner planet does not migrate in as far as desired. We have also moved the edge of the magnetospheric cavity out to a value of $a_R/2$. This halts the migration of the inward planet once it crosses into the cavity, but the inward migration is still halted by the reversal of the outermost planet when it hits a_R . Thus, the inner pair mass ratio falls somewhat short of the observed value, but does reproduce the qualitative features of the system in that the inner pair is wider than the 2:1 resonance while the outer pair lies between 3:2 and 2:1.

Of course, most planetary systems do not have masses measured to this accuracy, but our principal goal is not to constrain the histories of individual planets, but to understand the features of the underlying population of planetary systems. The most representative – in the sense of the most homogeneously selected – sample of low mass planets is that derived from the Kepler mission. Thus, we wish to compare our model to the corresponding sample of planetary systems detected with Kepler.

5.2. Kepler Analog Systems

As we can see from Figure 4, the degree of divergence of a planetary pair away from resonance is partially regulated by the mass ratio. Thus, to survey a realistic range of masses, we choose to simulate all mass combinations detected amongst Kepler triple systems. The Kepler results provide radii, not masses, so we must use an empirical mass-radius relation to convert each set of radii to masses. We use the results of Chen & Kipping (2018), which provides mass estimates for 7000 KOI, based on the model outlined in Chen & Kipping (2017). In particular, this model includes a spread in the expected masses at fixed radius, in accordance with the observational evidence. However, the possible spread in masses from planet to planet is quite large, and selecting three masses independently will give a large variation in mass ratios – inconsistent with the empirical peas-in-a-pod phenomenon (Weiss et al. 2018), which states that the degree of uniformity in planetary properties within a given system is smaller than that within the overall exoplanet population as a whole.

As a result, we choose the mass of the middle planet from the results of Chen & Kipping (2018) and then scale the inner and outer planets relative to this using the deterministic component of the mass-radius relation in Chen & Kipping (2017). This allows for some variation in the overall masses, but keeps the internal mass variation consistent with the radius variations. Using these

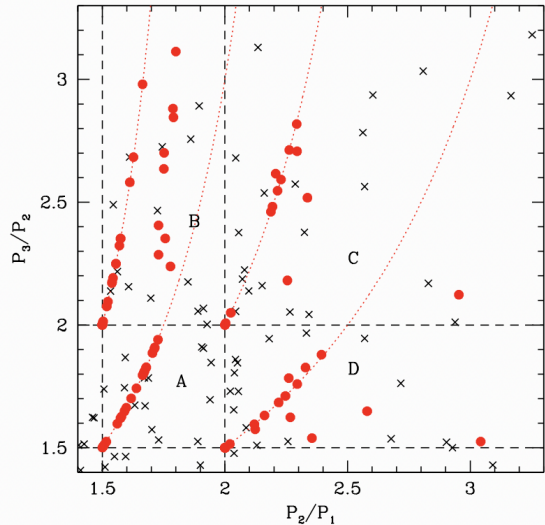


FIG. 10.— The solid red points represent the period ratios of inner (horizontal axis) and outer (vertical axis) pairs from our simulations of the set of Kepler triple analogues. The red dotted lines indicate the three-body relationship derived from eliminating the longitude of periastron of the middle planet. The crosses correspond to observed Kepler triples, and the dashed lines indicate the 3:2 and 2:1 commensurabilities. The labelling of the four quadrants A–D are discussed in the text.

masses we evolve forward realisations of the 107 Kepler planetary systems that contain three confirmed planets, none of which have a radius $> 6R_{\oplus}$ (our torque model is not applicable to planets of mass $> 30M_{\oplus}$ (Yu et al. 2023), which will open gaps in the protoplanetary disk). We wish to focus on the effects of the outspiral and detachment from the disk at late times, so we assume the planets occupy an initially compact configuration, starting the planets at 0.076 AU, 0.107 AU and 0.158 AU, so that the systems lie between the 3:2 and 2:1 resonances. Our model assumes a $1M_{\odot}$ planetary host star, as 85% of the 107 Kepler systems to which we compare orbit FGK stars.

The results of this parameter scan is shown in Figure 10. The crosses show the parameters of the known Kepler three planet systems – with inner pair period ratio on the horizontal axis and outer pair period ratio on the vertical axis. The solid red points show the results of the model calculations. We have divided this parameter space into four quadrants based on where the period ratios lie relative to the first order resonances ($q+1:q$). Systems in quadrant A have both pairs between the $q=1$ and $q=2$ first order resonances. Systems in quadrant B have a compact inner pair (between $q=1$ and $q=2$) and a wider outer pair (wider than $q=1$). Quadrant C has both pairs wider than the $q=1$ resonance and quadrant D has a wider inner pair (outside $q=1$) and a compact outer pair (between $q=2$ and $q=1$).

We see that our model is capable of producing systems that lie in all four quadrants, as well as a handful that cluster near the resonant chains. This variation is achieved solely as a function of the different masses – all of the red points are generated for the same disk evolution model, initial spatial configurations and a_R history. This demonstrates that the mass variations in the

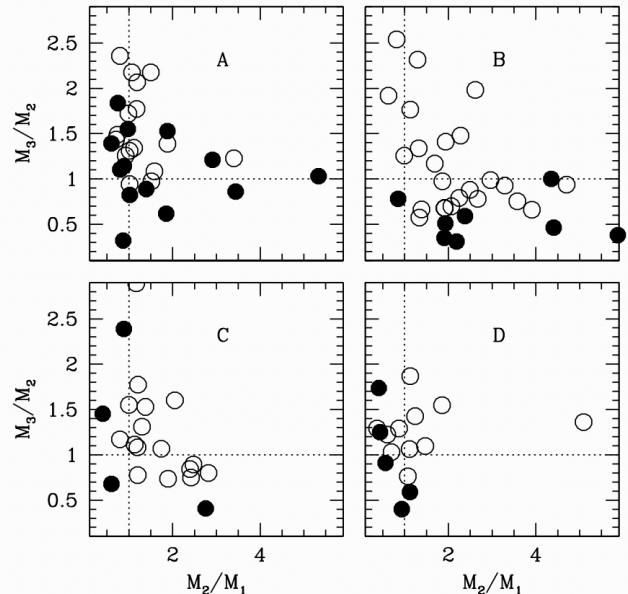


FIG. 11.— The four panels show the planetary mass ratios for model three planet systems that are found in each of the four quadrants identified in Figure 10. Those pairs denoted as solid points are still located close to a commensurability (within 1.50–1.55 or 2.00–2.05) at the end of the simulation, while those represented as open circles are well separated. The dotted lines indicate equal mass ratios for the inner pair (vertical) and outer pair (horizontal).

Kepler systems are capable of producing a substantial fraction of the overall period ratio variations. The red points in each quadrant also show an ordered structure in the immediate vicinity of each of the resonant intersections. These are the result of the fact that a resonant chain of two mean motion resonances also results in a three-body resonance, whose expression is derived by eliminating the longitude of periastron of the middle planet between the two resonances for which it is present (Aksnes 1988). These are shown as red dotted lines in Figure 10. It should be noted that our equations describe only the first order two-body resonant interactions and so do not contain any zeroth order contributions to the three-body resonance. Nevertheless, the diverging chains preserve the three body relationship well away from the two-body commensurabilities.

Figure 11 shows how the mass ratios influence the outcome of these models. It shows the distribution of mass ratios for model planetary systems in the four different quadrants. Objects in quadrant A tend to have the outermost planet larger than the middle planet, and those that are found far from resonance also tend to have the middle planet larger than the inner one. The planets in quadrant B tend to be found with middle planets larger than inner planets. Those planets in quadrant C tend to exhibit an overall trend of increasing mass outwards, while those in quadrant D tend to have inner pairs with similar mass ratios.

The examples shown in Figure 7 and Figure 8 demonstrate evolutionary pathways that lead to quadrants A and B. Figure 12 shows examples of systems that end up in the other two quadrants, this time drawn from the Kepler analogs. The left hand panel shows a relatively massive system, with planets of mass 8.1, 9.7 and 10.5

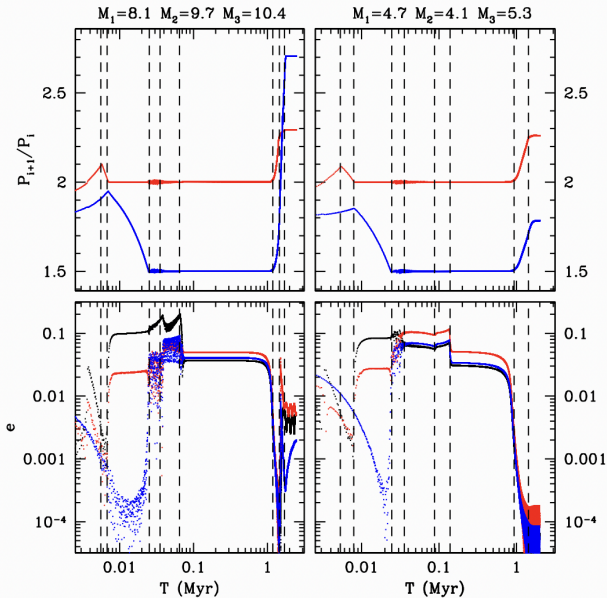


FIG. 12.— On the left hand side, $M_1 = 8.1M_\oplus$, $M_2 = 9.7M_\oplus$ and $M_3 = 10.4M_\oplus$. The colors identify the planets in the same way as in Figure 7. We see that this system starts in the same configuration as the system in Figure 7, but the outer planet diverges so far that it crosses the 2:1 resonance, leaving both pairs wide of the 2:1 commensurability and so located in quadrant C of Figure 10. In the lower left, we see that the divergence across the 2:1 resonance results in an eccentricity excitation. On the right hand side, we see the evolution of a three planet system with $M_1 = 4.7M_\oplus$, $M_2 = 4.1M_\oplus$ and $M_3 = 5.3M_\oplus$. In this case the inner pair traps into the 2:1 and the outer pair into the 3:2 resonance. Their eventual divergence leaves the system in quadrant D.

M_\oplus , a realisation of the masses in the system Kepler-60. It shows that the rapid inward migration causes the inner pair to diverge to the point that they are wider than the 2:1 resonance. When the inner planet halts this trend reverses and the inner pair lock into the 2:1 resonance. This also slows the inward migration of the middle planet so that the outer pair start to converge as well. However, this happens just before they diverge beyond 2:1, so that the convergence ultimately leads to their trapping in the 3:2 resonance. This transition leads to a period of dynamical rearrangement, as the inner pair loses its resonant lock, before the outer pair actually locks into the 3:2 resonance and only appears to settle down again once the outer planet reaches the torque reversal.

After this, the evolution is more stable, with a 2:1+3:2 chain evolving outwards until eventually the system diverges. The larger planetary masses means that the system takes longer to decouple, and the outer pair passes through the 2:1 resonance. The system doesn't trap because the evolution is divergent, but the resonant crossing does produce an eccentricity excitation (observed in the lower left panel) that doesn't entirely die away before the system completely freezes out. The end result is that neither pair remains in resonance at the end.

The right hand side of Figure 12 shows the evolution of a planetary system modelled after Kepler-295, with planetary masses of 4.7, 4.1 and 5.3 M_\oplus respectively, representative of a system that ends up in quadrant D. In this case, the evolution is quite similar to that seen in the left hand panel, with the inner pair captured into 2:1

after an initial divergence, and the outer pair captured into the 3:2, with a similar brief period of dynamical reshuffling. However, the outer planet is less massive in this case, and the system does not evolve far enough to pass through the 2:1 commensurability.

5.2.1. Initial conditions

Up to this point, we have assumed that the planets either formed close in or arrived from further out at an early stage, so that their final states are determined by the outward migration at late times. However, if the planets spiral in at later times, they may never reach the same compact configurations as we have simulated above.

Thus, to test this assumption, we have evolved the same 107 Kepler analog systems forward, but now starting them at semi-major axes of 0.16 AU, 0.29 AU and 0.54 AU. This does indeed lead to wider final configurations, as many systems get trapped in the 2:1 resonance during their inspiral, so that the detachment from resonance starts from a wider configuration. Furthermore, systems with low mass outer planets may never experience resonance locking because the inner planets migrate inwards faster and the outer planet cannot catch up before the disk evaporates. This can leave an inner pair near the resonance accompanied by a very wide outer pair – a system that will most often be observed simply as a double.

Figure 13 illustrates the effect of late time inspiral by showing the evolution of a system with the same mass configuration as in the right hand side of Figure 12, with the new, more distant, initial conditions. The inner planet reaches the torque reversal relatively early (at A), and the middle planet catches up to it at B. The systems started wider in this case and so both pairs capture into the 2:1 resonance at this point and the torques on the middle planet drive the pair inwards until the middle planet reaches the torque reversal at C. Eventually, the outer planet gets close enough to encounter the 2:1 resonance with the middle planet at D.

This causes some dynamical shake-up in the inner resonance but there is a period of time where both pairs librate in a 2:1 resonance, albeit with non-zero amplitudes and changes in configuration (E). Eventually the outer planet reaches the torque reversal (at F). This occurs late enough that the pairs immediately start diverging. Although both pairs pass through period ratio 2.25 (at G), they are already out of resonance at this stage, and end up freezing out at H. At this point the system is well located in quadrant C.

6. DISCUSSION

The results of § 5 demonstrate that our model results in the disruption of the majority of the resonant chains that form initially, in keeping with the qualitative features of the observed Kepler sample. To make a quantitative comparison, we must now compare the results of our simulations to the observations.

The Kepler satellite detects planets via their transits, so we must calculate the geometric probability that each of the planets in our simulations are actually observed. This scales as the inverse of the semi-major axis. The relative frequency of transit of members of multiple planet systems depends on the inclination dispersion within the

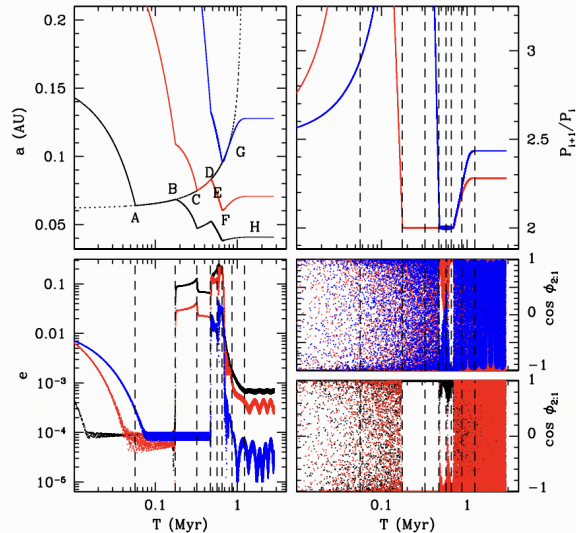


FIG. 13.— This three planet system is for $M_1 = 4.7M_\oplus$, $M_2 = 4.1M_\oplus$ and $M_3 = 5.3M_\oplus$. The resonant angles at the lower right are for the 2:1 resonance for the inner pair (upper panel) and outer pair (lower panel). The system gets trapped into a 2:1+2:1 resonant chain that eventually diverges to a final position in Quadrant C.

system. To assess these probabilities, we observe each system from 10^5 random orientations on the sky. For each realisation, the mutual inclinations are drawn from a Rayleigh distribution with an inclination dispersion of 3° , the upper limit consistent with the Kepler statistics (Fang & Margot 2012). The relative lines of nodes are assumed to be randomly distributed. With these results, we determine the relative frequency of observing all three planets in each system, and the frequency of observing the three different permutations of planetary pairs.

Figure 14 shows the resulting probability of observing different period ratios between neighbouring planets. In the upper panel, we show the observed distribution of Kepler period ratios, using those planets identified in the NASA Exoplanet Archive (Akeson et al. 2013) as confirmed, and discovered by Kepler. The resulting distribution resembles that of the standard compilation, from Fabrycky et al. (2014), but with improved statistics. The two first order resonances $(q+1)/q$, with $q=1$ and $q=2$, are shown as dashed lines, illustrating the well-known result that most nearest neighbour pairs in the Kepler sample are not near a commensurability.

The other panels in Figure 14 show the output from our simulations. The second panel from the top, labelled as ‘Original’, represents the results from our default simulations (the ones shown as red points in Figure 10). These have been assigned weights according to their geometric probability of observation, as discussed above. The third panel from the top represents the evolution of the same set of initial conditions, but with a_R scaled up by a factor of 1.2 relative to the default value given in equation (4). This represents the case of a stronger stellar magnetic fields. The resulting distribution is pretty similar, although the resonant peaks are less pronounced – i.e. a larger fraction of systems moved away from commensurabilities.

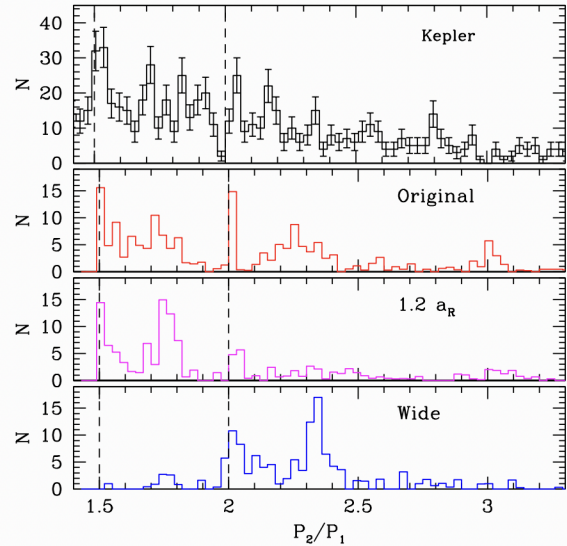


FIG. 14.— The upper panel shows the observed distribution of nearest neighbour period ratios in the sample of Kepler systems, based on the data from the NASA exoplanet archive, with Poisson error bars. The three panels below that show the outputs of our simulations. The second panel (red histogram) shows the final distributions of the simulations described in § 5.2, which assumes that all stars the default value of the transition radius a_R . The third panel (magenta histogram) shows the results of similar initial conditions, but using $a_R = 1.2$, so that the migration halts at longer orbital periods. The bottom panel (blue histogram) shows the results from the simulations that began with the more distant, and wider spaced, initial conditions discussed in § 5.2.1. This means that more systems get trapped into the 2:1 resonance instead of the 3:2 resonances, and the later divergence leads to wider systems. These simulations assume the standard a_R .

Finally, the lower panel shows the results of the simulations discussed in § 5.2.1. These start with more widely separated initial conditions (and an a_R corresponding to that of the second panel, i.e. all systems have the default a_R). We see that many more of these systems get captured in the 2:1 resonance and we get a distribution that skews to wider separations than seen in the observations.

The most important feature of this figure is that the simulations produce a similar fraction of systems wide of the commensurabilities as seen in the upper panel. The compact configurations produce a lot of systems between the $q=1$ and $q=2$ commensurabilities, while the more distant initial conditions primarily produce systems wide of the $q=1$ commensurability.

A more quantitative comparison of the non-resonant fractions is shown in Figure 15, which compares the cumulative distribution of period ratios between theory and observations, using the same colors as in Figure 14.

Thus, the black histogram represents the observed distribution drawn from the current Kepler sample (the solid histogram in the upper panel Figure 14). The red histogram represents the original model sample from the second panel, and which reproduces the observed distribution quite accurately. The magenta histogram shows the distribution from the third panel. This one shows too many at lower period ratios and too few at higher period ratios. The blue histogram shows the sample from the lowest panel – those drawn from wide initial conditions. In this case the model clearly produces too few close pairs

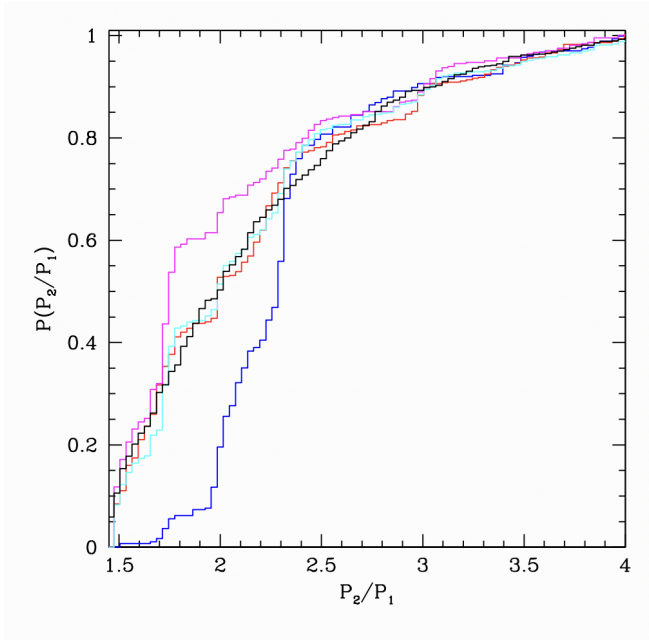


FIG. 15.— The black histogram shows the cumulative distribution of period ratios for the sample of current confirmed Kepler planetary systems – the summed version of the solid histogram in the upper panel of Figure 14. The red histogram shows the cumulative distribution from our default models – those shown in the second panel of Figure 14. The magenta histogram shows the models from the third panel of Figure 14, demonstrating that the simulations with larger a_R produce too many systems in compact configurations. The blue histogram represents the lowest panel in Figure 14 – those derived from the simulations that start with wide initial conditions. The cyan histogram represents a sample composed of 70% from the magenta histogram and 30% from the blue sample, indicating that this too can produce a reasonably accurate representation of the observations.

and even falls below the observed curve at larger periods, indicating a substantial pile-up of systems between period ratios of 2.2 and 3. Overall, we find that the default model does an excellent job of providing a distribution of period ratios broadly consistent with those observed. A Kolmogorov-Smirnov test indicates that the two distributions have a 70% chance of being drawn from the same underlying distribution. The observations can also be reproduced with combinations of the different samples. The cyan histogram shows a model in which 70% of the systems come from the simulations with larger a_R and compact initial conditions, along with 30% of the systems that began with wider initial conditions.

It is instructive to compare these results with those of prior related studies. The magnetospheric rebound model of Liu et al. (2017) describes a model of divergent migration driven by a one-sided torque exerted at the disk inner edge truncation, which can drive the outer planet away from an inner companion and break the resonance. Simulations of the Kepler population using this model (Liu & Ormel 2017) does indeed produce a population of non-resonant planetary pairs, but still leaves too many planets in resonant lock. Our model allows for multiple planets to experience outwardly directed migration, and the divergence arises when the relative rates of migration start to differ. Comparison of our simulation results with those of Liu & Ormel (2017) shows that our model produces more widely spaced systems and a much better agreement with observation, as shown in

Figure 15.

Another useful comparison set is the simulations of Izidoro et al. (2017) and Izidoro et al. (2021), the most comprehensive effort to date to compare the migration model with observations in a quantitative fashion. Izidoro et al. (2017) describe a model for the migration of low mass planets in both static and turbulent disks, which decay away on Myr timescales, leaving planets trapped in a chain of mean motion resonances. They furthermore run the simulations forward another 100 Myr after the dispersal of the gas disk, and track the evolution of systems that undergo dynamical instabilities which can break the resonant chains. The encouraging part of the results of Izidoro et al. (2017) is that the resulting instabilities do indeed produce many non-resonant systems. However, the fraction of resonant systems that remain is still far too high ($\sim 50\%$) and the dynamical instabilities lead to planetary collisions which result in systems too massive compared to the observed systems. The simulations of Izidoro et al. (2021) takes these models further by including a prescription for gas-assisted pebble accretion during the migration phase. Variation in the pebble flux and the formation time of planetesimals result in various levels of dynamical instability. The authors find that it is possible to match the neighbour period ratio distribution of the Kepler planets but, once again, only if one treats the fraction of unstable systems as a free parameter. For some parameter choices, most of the simulated systems do go unstable, but these also, once again, produce systems that are too massive.

Our results show that both of these problems can be alleviated with a more physically motivated inner boundary condition. We note that our approximate match to the observations in Figure 15 uses the full set of simulated systems, so that our remaining resonant fraction is consistent with observations. Furthermore, these results are achieved using planetary masses estimated directly from the observations, and so demonstrate that the period ratios and masses can be reproduced in a mutually consistent manner. This approach does leave open the question of how and where these planets assembled, but it demonstrates that their final orbital configurations are largely determined by the manner in which the disk evolves and dissipates.

The high multiplicity of these compact planetary systems has spurred many discussions regarding their dynamical stability. The question of whether the planetary systems are on the edge of dynamical instability is often expressed in terms of the planetary spacing as measured in terms of mutual Hill radii. It has been claimed that the Kepler multiplanet systems are close to being ‘maximally packed’ (Lovis et al. 2011; Fang & Margot 2013; Pu & Wu 2015), in the sense that they cannot be packed significantly closer without being dynamically unstable. Figure 16 shows the final spacings of our model three planet systems in terms of mutual radii. We see the final spacings of these planetary triples peaks between 10 and 20 Hill radii, which is similar to that estimated for Kepler systems.

For comparison, the dotted histogram shows the outcomes from the in situ assembly simulations of Hansen & Murray (2013) for the case of a total solid inventory of $20M_{\oplus}$. Both distributions show a broad spread around a single peak, displaced by a factor of a few from the

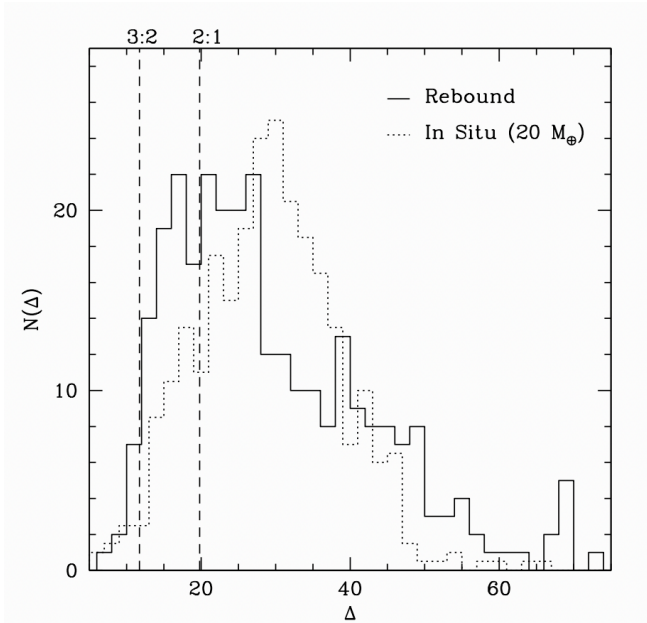


FIG. 16.— The solid histogram shows the spacings of the planets in our default set of Kepler analogue triples. The dotted histogram shows the mutual Hill spacings of planets emerging from the in situ simulations of Hansen & Murray (2013) (for a total solids inventory of $20 M_{\oplus}$). The two horizontal dotted lines indicate the spacings for a pair of $6M_{\oplus}$ planets in either the 3:2 or 2:1 resonance.

nominal stability limit (Pu & Wu (2015) and references therein). The magnetospheric rebound model actually produces systems that are even more compact than the in situ models, despite the fact that the latter are partially sculpted by considerations of dynamical stability, while the spacing of the former is regulated by the freeze-out process of the gaseous disk. As a consequence, it is misleading to infer that a closely packed planetary system is automatically the result of sculpting by late-stage dynamical instabilities.

The time at which a given planet freezes out of the migration will also determine the final orbital period of the planet. This will also be affected by the value of a_R and hence the stellar magnetic field. To test whether our model values are reasonable, we simulated the same 107 Kepler systems with the default value of a_R , a version with a_R scaled up by a factor 1.2 (discussed above already) and also one with a scaling factor of 0.8. Figure 17 shows the resulting distribution of final planetary locations for all planets summed over these three simulations. In this case we do not adjust the counts for the geometric probabilities because the observations to which we compare have already accounted for selection effects and purport to represent the true underlying distribution. The shaded regions are these corresponding observed trends in planet occurrence for Super-Earths, as measured by Petigura et al. (2018). The simulations provide an excellent match to the observed rise from short periods to a peak in the range of ~ 6 –8 days, followed by a drop-off towards larger periods. Immediately exterior to the peak, the simulations also match the slope measured by Petigura et al. (2018) but begin to drop below this at orbital periods >20 days. This is a reflection of our restriction to triple systems. Systems with additional planets are expected to further fill in the distribution at

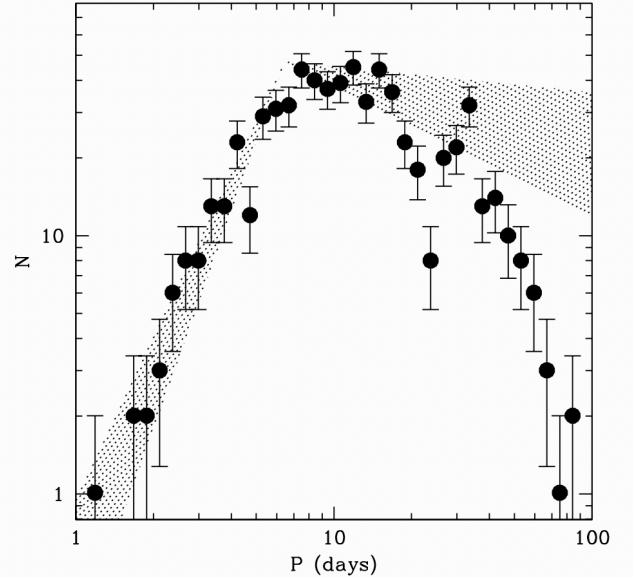


FIG. 17.— The solid points indicate the number of planets in our simulations that end their evolution at a given orbital period. The error bars are Poisson counting errors. The shaded regions indicate the observationally measured planetary occurrence rates for super-Earth planets from Petigura et al. (2018). The shaded regions indicate the range of slopes that lie within the observational uncertainties and the shaded regions have been scaled to match at the peak.

longer periods.

It is particularly noteworthy that the slope of the rise is matched well by these simulations. Previous attempts to explain this power law behaviour include connecting it to a range in stellar rotation rates (Lee & Chiang 2017) via a magnetically or centrifugally maintained disk inner edge (Koenigl 1991; Kenyon et al. 1996; Eisner et al. 2005). In the case of these calculations, it is determined by the mass distribution of the underlying planetary systems, which will determine the degree to which a planet is forced interior to the torque reversal and then when it freezes out.

7. CONCLUSIONS

The results presented here demonstrate that a detailed treatment of the inner boundary of protoplanetary disks (Yu et al. 2023) has a strong influence on the final configurations of planetary systems that migrate through this disk. In particular, these models show the existence of an inner transition region of outwardly directed migration, which causes divergent migration of planets in resonant chains at late times. This results in a substantial fraction of initially resonant chains diverging to the point that their period ratios no longer lie close to first order commensurabilities (although some may still be technically resonant because of their high precession rates). The resulting distribution of planetary neighbour period ratios is a good match to the observed distribution of planets detected by Kepler, and also provides a good match to the observed relative occurrence frequency of observed Super-Earth planets. These results provide an explanation for the long-standing problem that the observed distribution of period ratios showed far fewer resonant systems than expected in the models.

Our model is not as complete as some of the models that preceded it (Izidoro et al. 2017, 2021), in that we do not present a full description of planetary evolution and assembly from planetary embryo formation up to final planetary architecture. Rather, our model is designed to emphasize that some of the most important features of the observations (such as planetary orbital periods and neighbour period ratios) are likely to be the consequence of the structure of the inner protoplanetary disk, and how the planets evolve as the disk disperses. This is encouraging in the sense that it implies that the result is robust with respect to some of the poorly understood physics involved in the assembly and early evolution of planetary systems.

On a less optimistic note, the fact that the period ratio distribution does not depend sensitively on the assembly process reduces the ways in which we can probe

the formation conditions of planetary systems. It should be noted that our results match the observations if they begin with relatively compact configurations, so that examining the pathways to form the initial configuration may still provide a fruitful avenue of investigation. We will address this issue in a future publication.

Data availability: The data underlying this article will be shared on reasonable request to the corresponding author.

The authors thank the referees for prompt and comprehensive reports, which improved the exposition. This research has made use of the NASA Exoplanet Archive, which is operated by the California Institute of Technology, under contract with the National Aeronautics and Space Administration under the Exoplanet Exploration Program. This research has made use of NASA’s Astrophysics Data System Bibliographic Services.

REFERENCES

- Akeson R. L., et al., 2013, *PASP*, 125, 989
 Aksnes K., 1988, in Roy A. D., ed., *Long-term Dynamical Behaviour of Natural and Artificial N-body Systems*. pp 125–139
 Alexander R., Pascucci I., Andrews S., Armitage P., Cieza L., 2014, in Beuther H., Klessen R. S., Dullemond C. P., Henning T., eds, *Protostars and Planets VI*. pp 475–496 (arXiv:1311.1819), doi:10.2458/azu_uapress_9780816531240-ch021
 Batalha N. M., et al., 2013, *ApJS*, 204, 24
 Boley A. C., Morris M. A., Ford E. B., 2014, *ApJ*, 792, L27
 Borucki W. J., et al., 2010, *Science*, 327, 977
 Brasser R., Matsumura S., Muto T., Ida S., 2018, *ApJ*, 864, L8
 Chang S. H., Gu P. G., Bodenheimer P. H., 2010, *ApJ*, 708, 1692
 Chatterjee S., Tan J. C., 2015, *ApJ*, 798, L32
 Chen J., Kipping D., 2017, *ApJ*, 834, 17
 Chen J., Kipping D. M., 2018, *MNRAS*, 473, 2753
 Chiang E., Laughlin G., 2013, *MNRAS*, 431, 3444
 Choksi N., Chiang E., 2020, *MNRAS*, 495, 4192
 Coleman G. A. L., Nelson R. P., 2014, *MNRAS*, 445, 479
 Cossou C., Raymond S. N., Hersant F., Pierens A., 2014, *A&A*, 569, A56
 Coughlin J. L., et al., 2016, *ApJS*, 224, 12
 Damasso M., et al., 2023, *A&A*, 679, A33
 Donati J. F., et al., 2011, *MNRAS*, 417, 1747
 Eisner J. A., Hillenbrand L. A., White R. J., Akeson R. L., Sargent A. I., 2005, *ApJ*, 623, 952
 Fabrycky D. C., et al., 2014, *ApJ*, 790, 146
 Fang J., Margot J.-L., 2012, *ApJ*, 761, 92
 Fang J., Margot J.-L., 2013, *ApJ*, 767, 115
 Goldreich P., Schlichting H. E., 2014, *AJ*, 147, 32
 Hansen B. M. S., Murray N., 2012, *ApJ*, 751, 158
 Hansen B. M. S., Murray N., 2013, *ApJ*, 775, 53
 Hellary P., Nelson R. P., 2012, *MNRAS*, 419, 2737
 Ida S., Lin D. N. C., 2008, *ApJ*, 673, 487
 Ida S., Lin D. N. C., 2010, *ApJ*, 719, 810
 Izidoro A., Ogihara M., Raymond S. N., Morbidelli A., Pierens A., Bitsch B., Cossou C., Hersant F., 2017, *MNRAS*, 470, 1750
 Izidoro A., Bitsch B., Raymond S. N., Johansen A., Morbidelli A., Lambrechts M., Jacobson S. A., 2021, *A&A*, 650, A152
 Johns-Krull C. M., 2007, *ApJ*, 664, 975
 Kenyon S. J., Yi I., Hartmann L., 1996, *ApJ*, 462, 439
 Koenigl A., 1991, *ApJ*, 370, L39
 Lee E. J., Chiang E., 2017, *ApJ*, 842, 40
 Lissauer J. J., et al., 2011, *ApJS*, 197, 8
 Lissauer J. J., Rowe J. F., Jontof-Hutter D., Fabrycky D. C., Ford E. B., Ragozzine D., Steffen J. H., Nizam K. M., 2023, arXiv e-prints, p. arXiv:2311.00238
 Liu B., Ormel C. W., 2017, *A&A*, 606, A66
 Liu B., Ormel C. W., Lin D. N. C., 2017, *A&A*, 601, A15
 Lovis C., et al., 2011, *A&A*, 528, A112
 Masset F. S., Morbidelli A., Crida A., Ferreira J., 2006, *ApJ*, 642, 478
 Miranda R., Lai D., 2018, *MNRAS*, 473, 5267
 Murray C. D., Dermott S. F., 2000, *Solar System Dynamics*, doi:10.1017/CBO9781139174817.
 Passegger V. M., et al., 2024, arXiv e-prints, p. arXiv:2401.06276
 Petigura E. A., et al., 2018, *AJ*, 155, 89
 Press W. H., Teukolsky S. A., Vetterling W. T., Flannery B. P., 1992, *Numerical recipes in FORTRAN. The art of scientific computing*
 Pu B., Wu Y., 2015, *ApJ*, 807, 44
 Romanova M. M., Lovelace R. V. E., 2006, *ApJ*, 645, L73
 Romanova M. M., Lii P. S., Koldoba A. V., Ustyugova G. V., Blinova A. A., Lovelace R. V. E., Kaltenegger L., 2019, *MNRAS*, 485, 2666
 Terquem C., Papaloizou J. C. B., 2007, *ApJ*, 654, 1110
 Terquem C., Papaloizou J. C. B., 2019, *MNRAS*, 482, 530
 Tsang D., 2011, *ApJ*, 741, 109
 Villebrun F., et al., 2019, *A&A*, 622, A72
 Weiss L. M., et al., 2018, *AJ*, 155, 48
 Yu T. Y. M., Hansen B., Hasegawa Y., 2023, *MNRAS*, 523, 3569

APPENDIX

A: DYNAMICAL EQUATIONS

We wish to describe a system of three planets, subject to gaseous disk torques that cause migration in semi-major axis, and damping of eccentricities. The planets also interact gravitationally with their nearest neighbours, and our equations include the interactions with the first order resonances associated with the 2:1 and 3:2 commensurabilities.

The planetary dynamics will be described in terms of the orbital frequencies, n_1 , n_2 and n_3 , normalised to a fiducial value n_0 , so that $x_i = n_i/n_0$. These correspond to semi-major axis $a_1 < a_2 < a_3$, so that $\alpha_{12} = a_1/a_2$ and $\alpha_{23} = a_2/a_3$. Eccentricities are denoted by e_i and the arguments of periastron are designed as $\bar{\omega}_i$. We will incorporate effects of the first order resonances $(1+q)/q$ for $q = 1$ and $q = 2$, between nearest neighbours. The commensurate angles are $\psi_1 = 2\lambda_2 - \lambda_1$, $\psi_2 = 3\lambda_2 - 2\lambda_1$, $\psi_3 = 2\lambda_3 - \lambda_2$ and $\psi_4 = 3\lambda_3 - 2\lambda_2$. We normalise the timescale to $t_0 = M_*/(3n_0m_2)$,

so that $\dot{x}_i = dx_i/d\tau = t_0 dx_i/dt$. The resonant angles are constructed by combining these commensurate angles with the relevant longitudes of periastron.

The resulting evolutionary equations (Murray & Dermott 2000; Goldreich & Schlichting 2014; Terquem & Papaloizou 2019) for the x_i are

$$\dot{x}_1 = -x_1^2 \alpha_{12} [A_{12} \sin \psi_1 - B_{12} \cos \psi_1] - 2x_1^2 \alpha_{12} [C_{12} \sin \psi_2 - D_{12} \cos \psi_2] + \frac{3}{2} \frac{x_1}{\tau_{a,1}} + 3e_1^2 \frac{x_1}{\tau_{e,1}} \quad (\text{A1})$$

$$\begin{aligned} \dot{x}_2 = & 2x_2^2 \frac{m_1}{m_2} [A_{12} \sin \psi_1 - B_{12} \cos \psi_1] + 3x_2^2 \frac{m_1}{m_2} [C_{12} \sin \psi_2 - D_{12} \cos \psi_2] + \\ & -x_2^2 \alpha_{23} \frac{m_3}{m_2} [A_{23} \sin \psi_3 - B_{23} \cos \psi_3] - 2x_2^2 \alpha_{23} \frac{m_3}{m_2} [C_{23} \sin \psi_4 - D_{23} \cos \psi_4] + \frac{3}{2} \frac{x_1}{\tau_{a,1}} + 3e_2^2 \frac{x_2}{\tau_{e,2}} \end{aligned} \quad (\text{A2})$$

$$\dot{x}_3 = 2x_3^2 [A_{23} \sin \psi_3 - B_{23} \cos \psi_3] + 3x_3^2 [C_{23} \sin \psi_4 - D_{23} \cos \psi_4] + \frac{3}{2} \frac{x_3}{\tau_{a,3}} + 3e_3^2 \frac{x_3}{\tau_{e,3}} \quad (\text{A3})$$

and the coefficients A – D are functions of the eccentricity,

$$A_{ij} = f_1(\alpha_{ij})k_i + f_2'(\alpha_{ij})k_j \quad (\text{A4})$$

$$B_{ij} = f_1(\alpha_{ij})h_i + f_2'(\alpha_{ij})h_j \quad (\text{A5})$$

$$C_{ij} = f_3(\alpha_{ij})k_i + f_4(\alpha_{ij})k_j \quad (\text{A6})$$

$$D_{ij} = f_3(\alpha_{ij})h_i + f_4(\alpha_{ij})h_j \quad (\text{A7})$$

and the quantities f_i are the functions of the Laplace coefficients $b_i^{(j)}(\alpha)$, related to the expansion of the orbit-averaged disturbing function in terms of the resonant arguments. These are given by

$$f_1(\alpha) = -\frac{1}{2} \left(4 + \alpha \frac{d}{d\alpha} \right) b_{1/2}^{(2)}(\alpha) \quad (\text{A8})$$

$$f_2(\alpha) = \frac{1}{2} \left(3 + \alpha \frac{d}{d\alpha} \right) b_{1/2}^{(1)}(\alpha) \quad (\text{A9})$$

$$f_3(\alpha) = -\frac{1}{2} \left(6 + \alpha \frac{d}{d\alpha} \right) b_{1/2}^{(3)}(\alpha) \quad (\text{A10})$$

$$f_4(\alpha) = \frac{1}{2} \left(5 + \alpha \frac{d}{d\alpha} \right) b_{1/2}^{(2)}(\alpha) \quad (\text{A11})$$

$$f_2'(\alpha) = f_2(\alpha) - 2\alpha \quad (\text{A12})$$

$$f_2''(\alpha) = f_2(\alpha) - \frac{1}{2\alpha^2} \quad (\text{A13})$$

The quantities $\tau_{a,i}$ represent the eccentricity damping timescales given by equation (3), normalised to t_0 . The quantities $\tau_{e,i}$ represent the corresponding eccentricity damping timescales, taken to be $\tau_{e,i} = 0.03 |\tau_{a,i}|$ (after fitting to the calculations of Yu et al. (2023)). Eccentricity damping for a given planet i is switched off if $e_i < 10^{-4}$. This eccentricity damping can often lead to low eccentricities which, in turn, leads to high precession rates. As a result, some of the resonant angles can continue to librate even when the period ratios deviate from the exact commensurability. Our equations represent the expansions in terms of the resonant arguments for the instantaneous osculating value of α , and so we describe the functions f_j as functions of α and not simply a number at exact commensurability.

Another consequence of the low eccentricities is that it is prudent to replace e_i and $\bar{\omega}_i$ with h_i and k_i , defined as $h_i = e_i \sin \bar{\omega}_i$ and $k_i = e_i \cos \bar{\omega}_i$. The resulting evolutionary equations are

$$\dot{h}_1 = -\frac{h_1}{\tau_{e,1}} + \frac{\alpha_{12}}{3} f_1(\alpha_{12})x_1 \cos \psi_1 + \frac{\alpha_{12}}{3} f_3(\alpha_{12})x_1 \cos \psi_2 \quad (\text{A14})$$

$$\dot{k}_1 = -\frac{k_1}{\tau_{e,1}} - \frac{\alpha_{12}}{3} f_1(\alpha_{12})x_1 \sin \psi_1 + \frac{\alpha_{12}}{3} f_3(\alpha_{12})x_1 \sin \psi_2 \quad (\text{A15})$$

$$\begin{aligned} \dot{h}_2 = & -\frac{h_2}{\tau_{e,2}} + \frac{1}{3} \frac{m_1}{m_2} f_2''(\alpha_{12})x_2 \cos \psi_1 + \frac{1}{3} \frac{m_1}{m_2} f_4(\alpha_{12})x_2 \cos \psi_2 \\ & + \frac{\alpha_{23}}{3} \frac{m_3}{m_2} f_1(\alpha_{23}) \cos \psi_3 + \frac{\alpha_{23}}{3} \frac{m_3}{m_2} f_3(\alpha_{23})x_2 \cos \psi_4 \end{aligned} \quad (\text{A16})$$

$$\begin{aligned} \dot{k}_2 = & -\frac{k_2}{\tau_{e,2}} - \frac{1}{3} \frac{m_1}{m_2} f_2''(\alpha_{12})x_2 \sin \psi_1 - \frac{1}{3} \frac{m_1}{m_2} f_4(\alpha_{12})x_2 \sin \psi_2 \\ & - \frac{\alpha_{23}}{3} \frac{m_3}{m_2} f_1(\alpha_{23})x_2 \sin \psi_3 + \frac{\alpha_{23}}{3} \frac{m_3}{m_2} f_3(\alpha_{23})x_2 \sin \psi_4 \end{aligned} \quad (\text{A17})$$

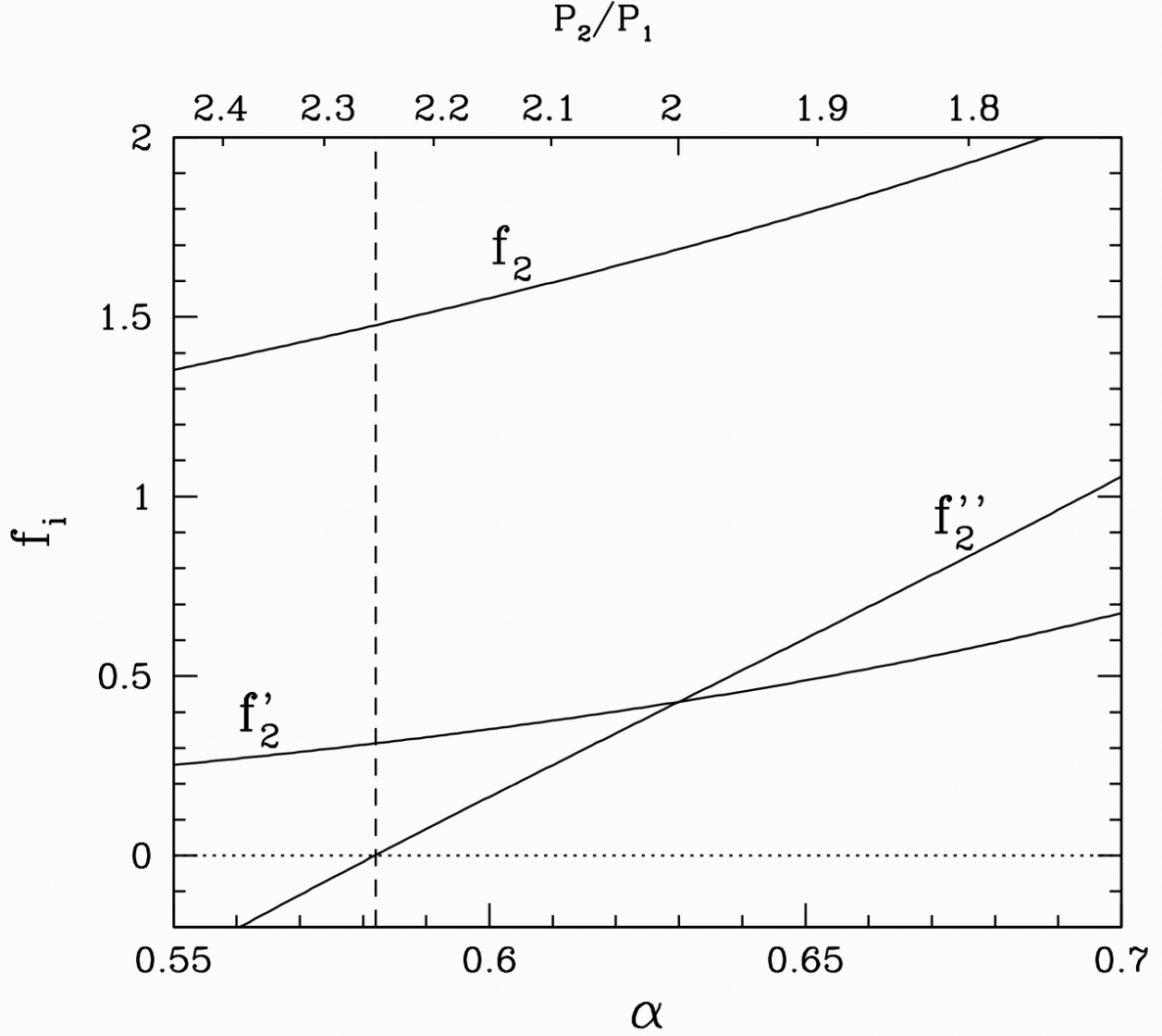


FIG. 18.— The solid curves indicate the functions $f_2(\alpha)$, $f'_2 = f_2 - 2\alpha$ and $f''_2 = f_2 - 1/(2\alpha^2)$. The vertical dashed line indicates the value of α at which f''_2 changes sign. The upper axis shows the corresponding period ratio, indicating that the zero occurs at $P_2/P_1 = 2.252$.

$$\dot{h}_3 = -\frac{h_3}{\tau_{e,3}} + \frac{1}{3}f''_2(\alpha_{23})x_3 \cos \psi_3 + \frac{1}{3}f_4(\alpha_{23})x_2 \cos \psi_4 \quad (\text{A18})$$

$$\dot{k}_3 = -\frac{k_3}{\tau_{e,3}} - \frac{1}{3}f''_2(\alpha_{23})x_3 \sin \psi_3 - \frac{1}{3}f_4(\alpha_{23})x_3 \sin \psi_4 \quad (\text{A19})$$

Finally, the above equations depend on the commensurabilities $\psi_1 = 2\lambda_2 - \lambda_1$, $\psi_2 = 3\lambda_2 - 2\lambda_1$, $\psi_3 = 2\lambda_3 - \lambda_2$ and $\psi_4 = 3\lambda_3 - 2\lambda_2$. The evolution of these variables is given by

$$\dot{\psi}_1 = \frac{1}{\Delta}(2x_2 - x_1) \quad (\text{A20})$$

$$\dot{\psi}_2 = \frac{1}{\Delta}(3x_2 - 2x_1) \quad (\text{A21})$$

$$\dot{\psi}_3 = \frac{1}{\Delta}(2x_3 - x_2) \quad (\text{A22})$$

$$\dot{\psi}_4 = \frac{1}{\Delta}(3x_3 - 2x_2) \quad (\text{A23})$$

where $\Delta = 3m_2/M_*$. The true resonant angles ϕ are determined by adding the relevant longitudes of periastron to the corresponding commensurabilities.

One technical detail that results from our use of the full functional form of $f_i(\alpha)$ is that the function f_2'' changes sign if $\alpha < 0.582$, which corresponds to a period ratio > 2.252 . This is shown in Figure 18 and is a consequence of the indirect contributions to the disturbing function. The sign of f_2'' determines the stable libration configuration of the 2:1 external resonance and so we see, in some of our results, a flip of the resonant libration as the period ratio increases. This only occurs if the resonance is well separated from the instability, which requires a fast libration and thus a small eccentricity. As a result, it is not clear this has an observable consequence but we include it for completeness.